LBL-11608 c.2
Preprint

Lawrence Berkeley Laboratory
UNIVERSITY OF CALIFORNIA

Submitted to Nuclear Physics

EVIDENCE FOR SPIN FLUCTUATIONS IN THE DEEP INELASTIC REACTION ^{165}Ho + ^{165}Ho AT 8.5 MeV/amu

R.J. McDonald, A.J. Pacheco, G.J. Wozniak,
H.H. Bolotin, L.G. Moretto, C. Schück, S. Shih,
R.M. Diamond, and F.S. Stephens

May 1981

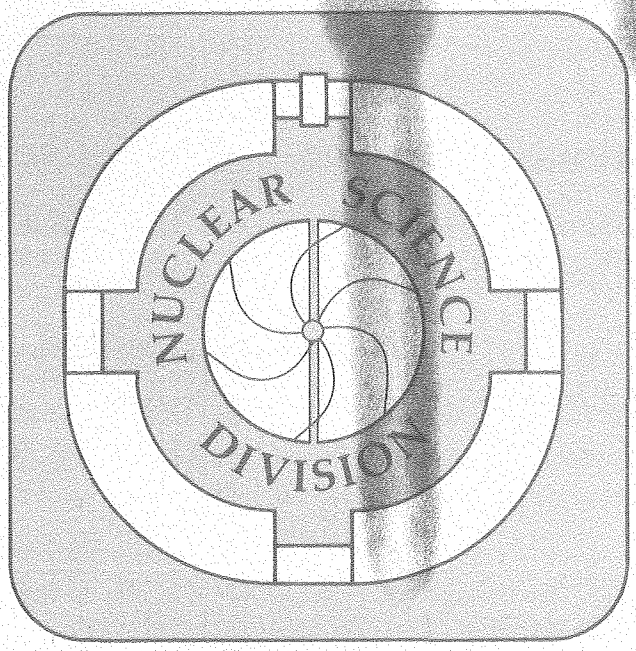

Prepared for the U.S. Department of Energy under Contract W-7405-ENG-48

DISCLAIMER

Evidence for Spin Fluctuations in the Deep Inelastic Reaction $^{165}Ho + ^{165}Ho$ at 8.5 MeV/amu*

R. J. McDonald, A.J. Pacheco[a], G.J. Wozniak, H.H. Bolotin[b], L.G. Moretto, C. Schück[c], S. Shih[d], R.M. Diamond, and F.S. Stephens

Nuclear Science Division
Lawrence Berkeley Laboratory
University of California
Berkeley, CA 94720

Abstract

Both the magnitude and alignment of the transferred angular momentum in the reaction $^{165}Ho + ^{165}Ho$ have been measured as a function of Q-value via continuum γ-ray multiplicity and anisotropy techniques. The spin transfer and the continuum γ-ray anisotropy increase throughout the quasielastic region. The spin transfer as a function of Q-value saturates at ~35$\hbar$/fragment, the anisotropy peaks at a value of ~2 and then decreases to near unity for the largest Q-values. The observed anisotropies are in good agreement with predictions from an equilibrium statistical model in which thermal excitation of angular-momentum-bearing collective modes and neutron evaporation give rise to in-plane components of the angular momentum.

Keyword Abstract

NUCLEAR REACTIONS: $^{165}Ho + ^{165}Ho$. Deep-inelastic reaction. E = 1400 MeV. Measured γ-ray multiplicity and anisotropy using continuum γ rays. Deduced $\langle I \rangle$, $\langle I_Z \rangle$, and P_{ZZ}. Theoretical interpretation based on a statistical equilibrium model.

*This work was supported by the Director, Office of Energy Research, Division of Nuclear Physics of the Office of High Energy and Nuclear Physics and Nuclear Sciences of the Basic Energy Sciences Program of the U.S. Department of Energy under Contract W-7405-ENG-48.

Permanent addresses

a) Comisión Nacional de Energía Atómica, Buenos Aires, Argentina
b) School of Physics, University of Melbourne, Parkville, Victoria 3052, Australia
c) Centre de Spectrométrie Nucléaire et de Spectrométrie de Masse, Orsay, France
d) Shanghai Institute of Nuclear Research, Shanghai, China

1. Introduction

During heavy-ion collisions, angular momentum is transferred from orbital motion to intrinsic degrees of freedom. Information regarding the mechanism inducing such a transfer can be obtained by determining the magnitude and alignment of the fragment spin as a function of Q-value. The correlation between spin transfer and energy dissipation has been experimentally investigated with both γ-ray multiplicity[1-9] (M_γ) and sequential-fission techniques[10-12]. These studies have shown that the mean transferred angular momentum increases with increasing Q-value until it saturates in the deep-inelastic region. In addition, anomalously large second moments of the γ-ray multiplicity distribution have been observed[6-8] in excess of those expected from a $2\ell + 1$ distribution.

The mean values of the transferred angular momentum can be explained in terms of frictional models. The anomalous widths can arise from various sources: on the one hand, mixing of entrance channel ℓ-values (ℓ-fractionation) may be responsible, while on the other hand, dynamic or statistical excitation of angular-momentum-bearing modes of the dinuclear system may be called into play. As an example of the former class, a large contribution to these widths can arise from diffusion along the mass asymmetry coordinate[9,13]. Similarly, in the latter class, a contribution of comparable magnitude can arise from thermal fluctuations in the angular-momentum-bearing modes[5,9,13-15] of the intermediate complex. This effect quantitatively accounted for the random angular momentum components deduced in the $^{20}Ne + {}^{63}Cu$ system[16].

Elementary dynamic considerations of the deep-inelastic reaction process (e.g. simple friction models) suggest that the transferred spin should be perpendicular to the reaction plane.[1] Angular momentum misalignment occurs

when in-plane components of angular momentum are present. These components can be generated either directly by some feature of the reaction mechanism, or by nonequilibrium or equilibrium statistical fluctuations in the angular-momentum-bearing modes of the intermediate complex. The γ-ray multiplicity distribution is sensitive only to fluctuations in the magnitude of the transferred spin. Information on the distribution of spin orientations may be obtained by measuring the γ-ray angular distribution, which is sensitive to fluctuations of the spin components.

Experimentally, large anisotropies (3-4) have been observed for discrete lines[17-19] from heavy-ion reaction products at small Q-values and substantially smaller anisotropies at larger Q-values. In contrast, for both light and heavy systems, only small anisotropies have been observed for the continuum γ-ray spectrum[1-6,18-21]. If there is a substantial admixture of dipole transitions in the predominantly quadrupole γ-ray cascade, a small anisotropy would be observed even if the fragment spins are perfectly aligned. This may be the dominant effect for light nuclei where the proportion of dipole transitions present in the continuum γ-ray spectra can be large. An alternative explanation is that these small anisotropies and associated large second moments are the result of random spin fluctuations[13-15,22,23] of either a quantal or thermal nature.

In the available continuum γ-ray studies, the evidence for the magnitude and nature of the spin fluctuations is not conclusive because of the small anisotropies observed, and because of uncertainties in the multipolarity of the continuum γ rays and in the corrections for particle emission. A more compelling case for the existence of spin fluctuation can be made if one chooses a system where the γ-ray anisotropy is observed to vary from small to large. Then, if the γ-ray multipolarity admixture is measured and corrections for the effects of particle emission are made, these changes in

the anisotropy can be related to corresponding variations in the spin alignment.

In this paper we report the simultaneous measurement of the magnitude and alignment of the transferred angular momentum in the 8.5 MeV/amu ^{165}Ho + ^{165}Ho reaction as a function of Q-value via continuum γ-ray multiplicity and anisotropy techniques. This system was chosen because large amounts of angular momentum can be transferred into the intrinsic spin (I) of these heavy rare-earth nuclei (see Table 1), which are known to have good rotational properties[24,25]. Furthermore, the steep mass-asymmetry potential for this symmetric system causes the reaction products to lie within a narrow range of Z-values centered around symmetry and minimizes ℓ-fractionation effects[9]. As a consequence, both of the essentially identical product fragments emit similar continuum γ-ray spectra which are strongly enriched in E2 transitions ($\gtrsim$80%) as discussed in sect. 3.

In sect. 2 the experimental apparatus and techniques are outlined. Continuum γ-ray spectra, average multiplicities $\langle M_\gamma \rangle$ and anisotropies as a function of Q-value are presented in sect. 3. In sect. 4, the data are analyzed in terms of a statistical model. Theoretical gamma-ray angular distributions are calculated incorporating the effects of misalignment and particle evaporation. A comparison between the model calculations and the data is made in sect. 5. This comparison demonstrates the existence of thermally induced random spin fluctuations. A brief report containing portions of this work has been published previously[26].

2. Experimental Technique

A beam of 8.5 MeV/amu ^{165}Ho ions from the Lawrence Berkeley Laboratory SuperHILAC was used to bombard a 0.85 mg/cm^2 self-supporting ^{165}Ho foil, oriented at 90° to the beam direction. Beam intensities of ~5 enA were

readily obtained on target. Particle singles and particle-γ coincidence data were accumulated event by event on magnetic tape.

2.1 Particle detectors

Reaction fragments were detected in three independent particle detection systems, placed at identical angles to the beam axis in two perpendicular planes, as shown in fig. 1. Two of these detection systems (1) and (2) consisted of a single 300-μm surface barrier detector, whereas the third contained an 11-μm ΔE detector in front of a 300-μm E detector. This telescope was used to monitor the width of the product mass distribution as a function of Q-value. Electropolished circular collimators were used both to eliminate detector edge effects, and to minimize slit scattering. Absorbers of 0.5 mg/cm^2 Au were placed in front of the Si detectors to shield them from low-energy electrons. The solid angles of the particle detectors were matched to ~5%.

Each particle detection system was aligned with a transit to better than 0.3° in both the horizontal and vertical directions. This alignment was verified at the beginning of the experiment by comparing the observed yields of elastic scattering at identical angles. Since the final beam collimator was 5 mm in diameter and 20 cm from the target, small changes in the beam position on the target were possible. These changes affected the scattering angle and therefore the scattered particle yields. During the experiment, the beam position was continuously monitored by comparing the left-right (detectors 1 and 3) and horizontal-vertical (detectors 1 and 2) yields of elastic scattering.

The particle detectors were calibrated using the kinematically calculated energy of the elastic peak. Corrections were made for pulse-height defect[27] and for energy losses due to the thicknesses of the target and absorber[28]. The linearity was verified using an electronic pulser.

2.2 γ-ray detectors

Unresolved γ rays emitted from the de-exciting fragments were detected in three electronically stabilized 12.7-cm diameter by 15.2-cm deep NaI detectors. Two of these detectors (1 and 3) were placed in the same horizontal plane as the particle detectors (1 and 3), and detector NaI(2) was placed in the same vertical plane as particle detector Si(2), as shown in fig. 1.

In order to improve the photopeak-to-Compton ratio, the NaI detectors were collimated to 8.0-cm diameter by means of 5-cm thick tapered Pb annuli. These detectors were placed 60 cm from the target in order to keep prompt γ-γ summing to <5% for events with multiplicities ~40. This 60-cm flight path also permitted the separation of neutrons from γ rays by time of flight as shown in fig. 2. Assuming a quasi-maxwellian distribution for the neutron energy, it is found that less than 5% of the neutrons had enough energy to arrive within the γ-ray time window.

The NaI detectors were calibrated for both energy and efficiency using cascade transitions in ^{60}Co, ^{88}Y, ^{152}Eu, and ^{207}Bi. A separate 7.6-cm x 7.6-cm NaI detector was set to trigger on one transition of the cascade, and the other transition was looked for in detector NaI(1, 2, or 3). The ratio of coincidences to singles, corrected for the γ-ray angular distribution, internal conversion and branching ratios, gave an absolute calibration for the γ-ray detection efficiency as a function of energy.

In addition, a Ge(Li) detector was placed in the horizontal plane to search for discrete transitions from product nuclei. Unfortunately, no discrete lines were observed due to the low overall coincidence efficiency of this detector and the variety of product nuclei formed. Continuum γ-ray anisotropy data obtained using this detector agreed with that from the NaI detectors.

2.3 System Geometry

In order to improve statistics and to reduce possible systematic uncertainties in the measured γ-ray multiplicity (M_γ) and anisotropy (A), a highly redundant detector geometry was utilized to obtain several independent measurements. Particle detectors Si(1), Si(2) and Si(3) together with the beam direction defined two mutually perpendicular reaction planes (see fig. 1).

Measurements of the average γ-ray multiplicity were made by taking the ratio between the yield from a NaI detector in coincidence with a Si detector ($Y_{\gamma_i - p_j}$) and the singles yield from the same particle counter (Y_{p_j}):

$$\langle M_\gamma \rangle \propto \frac{Y_{\gamma_i - p_j}}{Y_{p_j}} \quad . \tag{1}$$

The proportionality factor involves a correction for both the NaI efficiency and the angular distribution of the emitted γ-rays, $W(\theta)$, where θ is the angle between the γ-ray counter and the perpendicular to the reaction plane defined by the particle detector and the beam. Whenever the latter correction is not made, we will refer to "in-plane" or "out-of-plane" multiplicities, depending on whether $i = j$ or $i \neq j$ respectively. Four combinations were used in the evaluation of the multiplicity: (a) $Y_{\gamma_1 - p_1}/Y_{p_1}$, (b) $Y_{\gamma_2 - p_2}/Y_{p_2}$, (c) $Y_{\gamma_1 - p_2}/Y_{p_2}$ and (d) $Y_{\gamma_2 - p_1}/Y_{p_1}$. Combinations (a) and (b) gave in-plane measurements ($M_\gamma(90^\circ)$), whereas out-of-plane measurements ($M_\gamma(0^\circ)$) were obtained from (c) and (d).

Similarly, the anisotropy is calculated from the ratio between the in-plane and the out-of-plane yields of the γ-ray counters:

$$A = \frac{Y_{\gamma_i - p_i}}{Y_{\gamma_j - p_k}} \quad , \; j \neq k \quad . \tag{2}$$

In two cases, the combination of two γ-ray detectors in coincidence with one particle counter were considered ($Y_{\gamma_2-p_2}/Y_{\gamma_1-p_2}$ and $Y_{\gamma_1-p_1}/Y_{\gamma_2-p_1}$). These measurements were sensitive to the efficiency of the NaI detectors but were insensitive to differences in the solid angles, angular positions or gains of the Si counters. Two other combinations involved the use of one NaI in coincidence with two particle detectors ($Y_{\gamma_1-p_1}/Y_{\gamma_1-p_2}$ and $Y_{\gamma_2-p_2}/Y_{\gamma_2-p_1}$). In this case the results had to be corrected for differences in the singles yields of the Si detectors but they were insensitive to variations in the efficiency of the γ-ray detectors. To reduce both statistical and systematic errors, averages of the different types of measurements were used and the uncertainties reduced accordingly.

Particle detector 3, the ΔE-E telescope, was not utilized to measure either the multiplicity or the anisotropy due to the larger uncertainty in its energy calibration caused by the additional detector. NaI(3) was mainly used to assess the magnitude of the corrections resulting from the Doppler shift[29]. The detector combination Si(1)-NaI(3) gave rise to the largest correction. Doppler shift corrections for the other combinations were less than the statistical uncertainties. Data from NaI(3) (not shown) were also used to verify the in-plane isotropy of the γ-ray angular distribution and to obtain a 30° out-of-plane data point (Si(2), NaI(3)).

2.4 Electronics

To accumulate particle-γ coincidences and particle singles data, standard linear and logic electronic modules were used as shown in fig. 3. The logical "OR" of the constant-fraction timing signals from each of the three Si detectors was used to start four TACs. Each γ-ray detector stopped a separate TAC. Particle singles data could be "scaled down" by powers of two in order to reduce the density of singles events on magnetic tape. The

logical "OR" from these scale-down modules or the logical "OR" from the valid TAC outputs generated a "master gate" signal which opened all of the linear gates. Linear signals from each particle detector, each γ-ray detector, and each TAC were presented to a 16-channel multiplexer. Each of these 12 parameters was digitized sequentially in an 800-MHz ADC which was interfaced to a MODCOMP IV/25 computer in a direct memory processor mode. In addition, a "Tagword", constructed by different bits being set for each particle detector and valid TAC received, was appended to the stored event. Particle singles could be reconstructed by gating on proper values of the tagword.

2.5 Data acquisition and analysis

These 13-parameter event-by-event data were written on magnetic tape in 1000-word blocks via the program CHAOS[30], developed at this laboratory. The extensive monitoring features of this program, including gated spectra, were used to monitor proper operation of all detection systems throughout the experiment. A high-speed off-line sorting program[31] (EVA = EVent Analysis) was used to break out various subsets of the data. These results were displayed, printed, plotted and analyzed (e.g., summed, compressed, etc.) by the program SUSIE[32].

3. Experimental data

3.1 Particle energy spectra

Figure 4 shows the energy spectra obtained before (23°), at (27°), and behind (31°) the grazing angle (see Table 1). A strong elastic peak is observed before and at the grazing angle. The width of the elastic peak was determined mainly by the angular acceptance of the Si detectors, which was originally chosen to be ±3.4° for the 23° data. This resulted in a FWHM of ~60 MeV for the elastic peak. Since adequate beam current was available, the acceptance angle was decreased to ±2.2° for the 27° and 31°

data, thus improving the resolution to ~40 MeV. As was observed for other systems[33] with similar ratios of kinetic to Coulomb barrier energies, the broad quasi-elastic (QE) and deep-inelastic (DI) components overlap somewhat. This effect may be observed in the particle spectra as a function of lab angle (see fig. 4). At 23°, the quasi-elastic and deep-inelastic components form a wide shoulder on the elastic peak. At 31°, both the elastic and most of the quasi-elastic components have disappeared, leaving only the lower energy deep-inelastic peak.

3.2 γ-ray spectra

For nuclei at high spin, the many available decay paths dilute the intensity of discrete lines, and an unresolved spectrum is all that one observes even with a Ge(Li) detector. In order to understand the information content of these unresolved transitions, it is useful to plot the possible excitation energy vs angular momentum for a fragment produced via a deep-inelastic reaction. A schematic diagram of this E^* vs I plane and two examples of the subsequent decay for a quasi-elastic event (a) and a deep-inelastic event (b) are shown in fig. 5. Even for a fixed bombarding energy, a large region of the E^*-I plane can be populated in the $^{165}Ho + ^{165}Ho$ reaction process at 8.5 MeV/amu, as indicated by the closed curve in fig. 5. A much more restricted region is populated in a compound-nucleus reaction where the excitation energy is fixed by the beam energy (shaded area of fig. 5). For 27°, the projection on the E^* axis is shown to the left of this figure. An expanded view of the lower portion of the E^*-I plane indicates details of the γ-ray decay process.

For neutron-excess nuclei around mass 160, most of the available excitation energy is expected to be carried off by neutron emission. This process cools the nucleus, decreases its angular momentum, and introduces a

small random component in the spin distribution. Neutron evaporation proceeds until the so-called "entry limit"[25] (dashed) is reached, a region ~8 MeV above the yrast line (solid), below which γ-ray deexcitation starts to dominate. Because the entry limit and the yrast line are intrinsic nuclear properties, independent of the reaction mechanism, the subsequent γ-ray cascade from a DI product should be the same as that observed for the same compound nucleus product[25,34-36]. These transitions can be divided into two types, as shown in the lower part of fig. 5. The "statistical" transitions cool the nucleus with little or no loss of angular momentum, while the yrast and yrast-like transitions are mainly stretched E2 γ-rays which reduce the nuclear spin and carry off excitation energy. From compound nucleus studies, the statistical transitions have been shown to be predominantly a mixture of stretched and non-stretched E1 transitions[37] whose intensity falls off exponentially with increasing γ-ray energy above 2 MeV. For deformed nuclei the yrast and yrast-like transitions[34] are predominantly stretched E2 γ-rays which form a "bump" in the energy spectra below ~2 MeV.

Figure 6(a) shows an in-plane and an out-of-plane γ-ray energy spectrum in coincidence with DI fragments at 27° and for a Q-value gate of -148 MeV < Q < -103 MeV. A comparison between the in-plane and out-of-plane spectra shows that the high-energy region (2-5 MeV) is essentially isotropic, whereas the low-energy region contains a "bump" which is significantly more pronounced in plane. These spectra can be interpreted as follows: The isotropic high-energy tail is caused by statistical transitions. The bump is caused by the yrast-like and yrast transitions, and their in-plane dominance is due to the fact that for nuclei whose spins are nearly aligned perpendicular to the reaction plane, the stretched E2 angular distribution peaks in plane.

In-plane γ-ray spectra, normalized so that the integral of each curve is equal to the average multiplicity $\langle M_\gamma \rangle$, are shown in fig. 6(b) for several Q-value regions. In each of these spectra there is an obvious E2 bump whose high-energy edge moves to higher energies as the Q-value increases. Within the deep-inelastic region (-400 MeV < Q < -150 MeV) the upper edge of the E2 bump is constant. Since $E_\gamma \propto I$ for rotational nuclei, the γ rays deexciting the states of highest spin occur on the upper edge of the E2 bump. The edge of the bump, by moving to higher energies with increasing Q-value, implies that the spin transfer also increases. For very large Q-values where the upper edge of the bump is stable, the spin transfer has saturated. This dependence of spin transfer on the reaction Q-value is seen more clearly in the γ-ray multiplicity data presented in sect. 3.4.

Recent studies of unresolved γ-ray energy spectra from compound nucleus reactions have shown that these spectra contain quantitative information on the number of statistical transitions in the γ-ray cascade[38]. Figure 7 indicates how the number of statistical transitions was extracted by fitting the data with the empirical form[e] of the E1 spectrum

$$P(E_\gamma) = CE_\gamma^2 \exp(-E_\gamma/T) \qquad (3)$$

where T is an effective temperature which turns out to be 0.6 MeV and C is a normalization constant. The integral of $P(E_\gamma)$, normalized to fit the data at

---

e) The value of the exponent used is a subject of controversy, as discussed in ref. 38). Our results would not differ significantly even if values of 3, 4, or 5 were used instead of 2, particularly since we exclude the low energy γ-rays.

E_γ > 2 MeV, equals the number of statistical transitions in the spectrum (two times the number per fragment). These results as a function of Q-value are tabulated in Table 2. Over the Q-value region -60 MeV to -425 MeV, the fraction of statistical transitions is nearly constant (~17%). However, the number of these E1 transitions per fragment increases from 1.5 to 2.7. Recent results from compound nucleus studies also demonstrate that the number of statistical transitions increases with the excitation energy of the product nucleus[38].

3.3 "Raw" vs "unfolded" γ-ray spectra

Although the collimated large-volume NaI detectors used in this experiment exhibited good photopeak-to-total ratios (~50%), the energy spectra were still contaminated by Compton events. The "raw" spectra were "unfolded"[39] utilizing the measured response function of the detector and a 0.3-MeV lower threshold. This produces an efficiency-corrected unfolded spectrum. The raw γ-ray energy spectra resemble the unfolded spectra very closely as is shown in fig. 8.

For the 27° data, values of $\langle M_\gamma \rangle$ and anisotropy were obtained for both raw and unfolded data and were found to be identical within experimental uncertainties. Consequently, data from the other angles were not unfolded, and no distinction will be made between raw and unfolded data in the remainder of this paper.

3.4 γ-ray multiplicity.

Studies of compound nuclei have shown that within the heavy rare-earth region of the periodic table, the average γ-ray multiplicity $\langle M_\gamma \rangle$ is linearly related to the nuclear spin[24,40]. Consequently, for DI reactions in which both fragments are in the heavy rare-earth region, $\langle M_\gamma \rangle$ is linearly related to $\langle I_1 \rangle + \langle I_2 \rangle$. Figure 9 (top row) shows the measured

values of the in-plane multiplicity ($M_\gamma(90^\circ)$) and the out-of-plane multiplicity ($M_\gamma(0^\circ)$). A strong enhancement of γ rays in the reaction plane is observed for most Q-value regions. This enhancement is due to the fact that the nuclear spin is nearly aligned perpendicular to the reaction plane and thus produces an in-plane peaking of the γ-ray intensity for stretched E2 transitions. The angle-integrated γ-ray multiplicity $\langle M_\gamma \rangle$ (solid line) was derived from $M_\gamma(90^\circ)$ using the angular distribution function described in sect. 4. For particles detected at 23°, 27° and 31° (top row, fig. 9), the γ-ray multiplicities have similar values and rise rapidly with increasing Q-value in the QE region, peak in the DI region, and decrease somewhat for very large Q-values.

Figure 9 (center row) shows the fragment spin immediately prior to γ-ray emission (solid lines) for each of the three angles. These fragment spins were deduced from the γ-ray multiplicities as follows:

$$\langle I \rangle = \langle M_\gamma \rangle + 2H - 2b \qquad (4)$$

where $\langle I \rangle$ is the average spin for one of the fragments, $\langle M_\gamma \rangle$ is the angle-integrated average γ-ray multiplicity for both fragments, H is the number of transitions per fragment hidden below the 0.3 MeV threshold (set off-line to exclude backscatter events), and b is the number of statistical transitions per fragment extracted from the analysis of the γ-ray energy spectrum (see sect. 3.2 and Table 2). The value of H was estimated to be three by inspection of the decay schemes[41] for nuclei with mass numbers between 150 and 165. To determine the fragment's spin before neutron emission, the spin derived from the measurement of $\langle M_\gamma \rangle$ was corrected for the angular momentum carried away by evaporated neutrons[42]. The dashed line in fig.

9(b) represents the pre-neutron emission spin values. The rapid rise of fragment spin with increasing Q-value indicates that the angular-momentum transfer is strongly coupled to the energy dissipation process.

3.5 Gamma-ray anisotropy

For a perfectly aligned system, the stretched E2 angular distribution[43] with respect to the direction of the nuclear spin is given by

$$W_{E2} = \frac{5}{4}\left[1 - \cos^4\alpha\right] \quad . \tag{5}$$

This expression is normalized such that $\int W_{E2}(\alpha)d\Omega = 4\pi$. For a pure E2 cascade and a perflectly aligned system the anisotropy $[W_{E2}(90^\circ)/W_{E2}(0^\circ)]$ is infinite.

Measured values of the γ-ray anisotropy for 0.6 MeV $< E_\gamma <$ 1.2 MeV are shown in fig. 9. This restriction on E_γ enhances the γ-ray anisotropy since this region is strongly enriched in E2 transitions (~90%). For all three particle detection angles, the Q-value dependence of the anisotropy is similar. In the QE-region, the anisotropy rises with increasing Q-value and peaks at a maximum value of ~2.2. In the DI-region, the anisotropy decreases with increasing Q-value and approaches unity at the highest Q-value. The poor statistics of the 31° data is due to the fact that at this angle the QE-region is only weakly populated and that only one combination of detectors provided us with anisotropy data compared to four combinations at the other angles.

Comparing the Q-value dependence of <I> and of the anisotropy, one observes that both the anisotropy and <I> increase through the QE-region, while the anisotropy decreases and <I> saturates in the DI region. The initial rise of both the spin transfer and the anisotropy indicates that during the early stages of energy damping there is a rapid buildup of

aligned spin, as predicted by friction models. The subsequent fall of the anisotropy at larger Q-values suggests that the aligned component of the transferred spin has saturated or is decreasing, whereas randomly oriented components continue to increase.

4. Theoretical Considerations

In order to calculate a theoretical radiation pattern to compare with the experimental anisotropy data, we must analyze the entire reaction and deexcitation process. It is useful to divide this process into three time frames as shown in fig. 10. Within the first time period ($\sim 10^{-21}$ sec), some energy of relative motion is transferred into excitation energy (E^*) and some orbital angular momentum (L) is transferred into intrinsic spin of the fragments. Although friction models predict that the transferred spin is aligned perpendicular to the reaction plane, several experimental studies have indicated a depolarization effect[2,5,6,20] that occurs on the same time scale as the heavy-ion interaction time. This "primary" depolarization effect may be associated with different physical causes[13-15,22,23], e.g., dynamical processes, quantal fluctuations and nonequilibrium or equilibrium statistical effects. In this paper, we will interpret the data in terms of the statistical equilibrium model of Moretto and Schmitt[15] which represents the long-time limit which all other models should approach.

After the rotating dinuclear system separates, the excited nuclei undergo particle emission as depicted in the second time region shown in fig. 10 ($\sim 10^{-19}$ to 10^{-16} sec). Within this time frame, the product nuclei undergo particle decay, mainly neutron emission. The emission of

neutrons decreases the average fragment spin $\langle I \rangle$, decreases its z-component $\langle I_z \rangle$, and adds a neutron-induced dispersion, σ_n, to the spin components. These effects cause an additional "secondary" misalignment of the fragment's spin.

The third time region shown in fig. 10 ($\sim 10^{-12}$ to 10^{-9} sec) is dominated by γ-ray deexcitation. The experimental observables, namely the γ-ray energy spectra, multiplicities, and anisotropies, are generated during this time frame. The magnitude and direction of the fragment spin immediately prior to γ-ray emission is determined by the primary and secondary misalignment mechanisms. Thus, in order to study any "primary" depolarization, we must understand time frames II and III well enough to relate the observables (time frame III) to effects which occurred during time frame I.

4.1 Primary Spin Misalignment Mechanism

The spontaneous fission of $^{252}Cf(J^{\pi} = 0^{+})$ produces fragments which have ~7-8$\hbar$ of angular momentum oriented perpendicular to the fission axis[44]. This angular momentum is most likely generated by the bending oscillations of the fissioning nucleus. Recently, Berlanger et al.[2] proposed that the same effect may arise during the primary deep-inelastic reaction process. More generally, Moretto and Schmitt[15] have proposed that a number of thermally excited angular-momentum-bearing collective modes associated with the dinuclear complex (wriggling, tilting, bending, and twisting) generate randomly-oriented components of angular momentum. This model describes the rotating dinuclear system in terms of two equal touching spheres whose internal degrees of freedom are equilibrated during the nuclear interaction time, labeled time frame I on fig. 10. The resulting equilibrium probability distribution for the spin components of the fragments is

$$P(I_x,I_y,I_z) \propto \exp\left[-\frac{I_x^2}{2\sigma_x^2}-\frac{I_y^2}{2\sigma_y^2}-\frac{(I_z-\langle I_z\rangle)^2}{2\sigma_z^2}\right] \tag{6}$$

where the coordinate system is defined such that the z-direction is perpendicular to the reaction plane, and the x-direction is the line between centers at the time of separation.

The variances for the three coordinates are related to the rigid-body moment of inertia ($\mathcal{J}$) for one fragment and the nuclear temperature (T). For a symmetric exit channel and two touching spheres the three variances are[15,45]

$$\begin{aligned}\sigma_x^2 &= \frac{6}{5}\mathcal{J}T\\ \sigma_y^2 &= \frac{6}{7}\mathcal{J}T\\ \sigma_z^2 &= \frac{6}{7}\mathcal{J}T \quad .\end{aligned} \tag{7}$$

4.2 Secondary Spin Misalignment Mechanism

During time frame II, the nucleus cools by emitting neutrons. To obtain the average number of neutrons emitted <n>, we assumed that one neutron is emitted for each 12 MeV of excitation energy above the yrast line. Neutron evaporation decreases the nuclear spin <I> and increases its dispersion σ. Neutron evaporation corrections[f] were calculated using the method of ref. 42).

---

f) Very little charged particle emission is expected, possibly ~0.1 α-particle per reaction. According to the model of Blau and Moretto[42], this would not significantly affect the results, particularly since any α-particle emission would result in less neutron emission.

4.3 Spin Probability Distribution Function

For two equal touching spheres the three variances are approximately equal as indicated by eq. (7):

$$\sigma_x^2 \simeq \sigma_y^2 \simeq \sigma_z^2 \simeq \sigma T \equiv \sigma_{th}^2 \quad . \tag{8}$$

The variance σ_n^2 associated with neutron emission is added in quadrature to the thermally induced σ_{th}^2 producing an overall variance σ^2. The other parameter needed to define the spin distribution function is the average aligned component $\langle I_z \rangle$. Its value is deduced from the experimental value of $\langle I \rangle$ (eq. 4) using

$$\langle I \rangle = \int I \; P(I_x, I_y, I_z) \, d^3I \tag{9}$$

which yields, explicitly

$$\frac{\langle I \rangle}{\langle I_z \rangle} = \sqrt{\frac{2}{\pi}} \frac{\sigma}{\langle I_z \rangle} \exp\left(- \frac{\langle I_z \rangle^2}{2\sigma^2} \right) + \left(1 + \frac{\sigma^2}{\langle I_z \rangle^2} \right) \operatorname{erf}\left(\frac{\langle I_z \rangle}{\sqrt{2}\sigma} \right) \quad . \tag{10}$$

4.4 γ-ray Angular Distributions

Using the above spin probability distribution function, a theoretical expression for the continuum γ-ray angular distribution has been derived in detail in ref. 45). Thus, only a brief sketch of the derivation is given below.

For an ensemble of aligned nuclei, decaying via stretched E2 transitions, the angular distribution $W_{E2}(\alpha)$ is given by eq. (5). If a distribution of spins is considered, $W_{E2}(\alpha)$ must be folded into this spin probability

distribution function. The angle α between the direction of a spin vector and the direction of observation may be expressed in terms of the polar coordinates of the spin θ',ϕ' and those of the observation direction θ,ϕ. The resulting angular distribution is given by

$$W'_{E2}(\theta,\phi) = \int W_{E2}[\alpha(\theta,\phi,\theta',\phi')]\, P(I',\theta',\phi')\, d^3I' \quad . \tag{11}$$

Using the distribution function given by eq. (6), the resulting angular distribution $W_{E2}(\theta,\phi)$ depends on the parameter $\sigma^2/\langle I_z\rangle^2$. Since some fraction f of the total number of γ rays is composed of isotropic transitions, the final angular distribution becomes

$$W(\theta,\phi) = (1 - f)W'_{E2}(\theta,\phi) + f \quad . \tag{12}$$

4.4 Model calculations

In order to calculate the thermal variance (eq. 8), the moment of inertia is calculated assuming that each fragment is a rigid sphere of radius $r = 1.2\ A^{1/3}$ where A is the mass number of the fragment. The temperature is calculated from the excitation energy ($E^* = -Q/2$) and the rotational energy (E_R) by

$$E^* - E_R = aT^2 \tag{13}$$

where "a" is the level density parameter taken to be A/8.

The calculation proceeds iteratively from the following inputs: the γ-ray multiplicity at 90° ($M_\gamma(90°)$), the number of E2 transitions below the 0.3-MeV threshold (estimated to be three), the number of statistical transitions (obtained from the data) and the Q-value. Within

this iteration loop, σ^2, $W(\theta,\phi)$, $\langle M_\gamma \rangle$, $\langle I_i \rangle$ (spin before neutron evaporation), $\langle I_f \rangle$ (spin after neutron evaporation), $\langle I_z \rangle$, E_R, and $\langle n \rangle$ are calculated. These values are then used to calculate the anisotropy.

5. Discussion

5.1 γ-ray anisotropy

Figure 11 shows experimental values of the anisotropy for $E_\gamma > 0.6$ MeV compared to several stages of the model calculation. The solid line represents the complete calculation, including both the primary and secondary depolarizations and the measured fraction of statistical transitions. This calculation reproduces the increasing anisotropy in the QE region, its peaking, and subsequent decline in the DI region. The lower cutoff of 0.6 MeV γ-ray energy was selected for comparisons with the model since additional uncertainties (e.g., possible loss of alignment due to hyperfine interaction) are associated with these low energy γ-rays[46].

In order to illustrate the relative importance of the primary and secondary depolarization mechanisms, the input conditions were changed to simulate the different misalignment sources. The calculation which omits both the primary and secondary depolarization processes (dashed line) illustrates the effect that statistical (E1) transitions have in reducing the anisotropy from infinity, the value expected for pure E2 transitions. This calculation overestimates the data by almost a factor of three. If the misalignment due to neutron evaporation is also included, the calculated anisotropies decrease (dotted line) but still overstimate the data by a factor of two. After adding the thermal misalignment, the calculation (solid line) is in good agreement with the data. The uncertainties in the calculation were estimated from realistic variations of the input parameters (sect. 4.4) and were found to be of the same magnitude as those shown for

the data points. In these calculations σ_{th} is scaled down as $\langle I_z \rangle$ decreases due to neutron emission. This correction was not included in a previous calculation[26].

In light of the agreement between the model calculation and the data, it is instructive to see if the model can reproduce data for a similar symmetric system. Aguer, et al.[20] measured continuum γ rays from symmetric fragments of mass ~160 produced in the $^{136}Xe + ^{197}Au$ reaction at 7.8 MeV/amu. Because of the large mass transfer required to reach symmetry, symmetric fragments were only observed at large Q-values. Using their measured values[20] for $\langle M_\gamma \rangle$ and Q, our model predicts an anisotropy of ~1.5 which agrees well with their measured anisotropy of 1.4 ± 0.2 for the Q-value region -280 MeV $< Q <$ -140 MeV.

The γ-ray anisotropy has been measured for several other systems[2-6,17-19,21] having asymmetric final states. In its present form, the model cannot be used to calculate the anisotropy for these systems. However, these data generally exhibit qualitative features similar to those obtained for the Ho + Ho system. For example, continuum γ rays from the system Kr + Er by Puigh et al.[21] showed a similar dependence of the anisotropy on Q-value. A peak value of ~1.46 was observed for the continuum γ-ray anisotropy. This peak value is smaller than that observed for the Ho + Ho system, possibly due to a smaller fraction[24,40] of stretched E2 transitions being emitted from products from the Kr + Er system. Discrete γ-ray transitions from this system yielded larger anisotropies (~2) but with large uncertainties.

Measurements of discrete γ rays from the system $^{16}O + ^{48}Ti$ by Puchta et al.[19] revealed a similar trend for the anisotropy vs Q-value. For this light system, a large peak anisotropy (~4) was observed at low Q-values (~-30 MeV) which decreased to unity by -50 MeV.

5.2 Spin Alignment

The understanding of the degree of spin alignment in terms of the measured anisotropy is somewhat obscured by the highly nonlinear relationship between them. A better insight into the physical situation can be obtained through the evaluation of quantities more directly related to the spin distribution itself. Among them, the most significant are the average aligned component of the spin ($\langle I_z \rangle$), the variance (σ^2), and the alignment parameter P_{zz} defined as

$$P_{zz} = \frac{3}{2} \frac{\langle I_z^2 \rangle}{\langle I^2 \rangle} - \frac{1}{2} \quad . \tag{14}$$

Note that P_{zz} ranges from 1 for a perfectly aligned system to 0 for the case of complete misalignment.

In fig. 12, three different curves of P_{zz} as a function of Q-value, corresponding to different situations, are shown. The dashed line was calculated including only the effect of thermal misalignment ($\sigma_{th}^2 \neq 0$, $\sigma_n^2 = 0$). This curve describes the alignment of the system after the collision process itself and before the decay by neutron emission. The alignment increases rapidly across the quasielastic region and then falls slightly at higher Q-values. This behavior is interpreted as follows: At small Q-values little or no angular momentum goes into intrinsic spin of the fragments, and consequently there is little spin alignment. For more inelastic collisions a progressively larger amount of angular momentum is converted into spin, which is preferentially aligned perpendicular to the reaction plane. For even larger Q-values, the thermal production of randomly oriented components dominates, causing a slow decrease in the alignment.

A similar interpretation applies to the behavior of P_{zz} after neutron emission (solid curve). Since neutron emission increases the spin misalignment, and the number of emitted neutrons increases with Q-value, the fall of the alignment for large Q-values is more pronounced. This divergence of the two curves at large Q-values reflects the importance of the secondary misalignment in explaining the observed large decrease in the anisotropy across the DI region. It should be noticed that this result is not in contradiction with our previous statement on the relative importance of primary and secondary misalignments. Indeed, for very inelastic events, neutron emission signficantly decreases the anisotropy. However, the magnitude of the anisotropy is still controlled by the primary process as discussed in section 5.1 and illustrated in fig. 11. To make this point clear, the dotted curve in fig. 12 shows the expected values of P_{zz} if one assumes that neutron emission is the only source of misalignment ($\sigma_{th}^2 = 0$, $\sigma_n^2 \neq 0$). A comparison between the dashed and the dotted curves shows that the thermal process is significantly more effective in destroying perfect alignment.

Further insight into the angular-momentum transfer process is obtained from the behavior of the different spin components as a function of Q-value. In fig. 13, curve 1 shows the magnitude of the total spin before neutron emission as deduced from the γ-ray multiplicity data. Curves 2 and 4 represent the evolution of $\langle I_z \rangle$ (the aligned component of the spin) and σ_{th} (the square root of the thermal variance) respectively. The three curves together (1, 2 and 4) show the relative contribution of the aligned and misaligned components to the pre-neutron-emission value of total spin as given by eq. (10). For the quasielastic region, as the Q-value increases, $\langle I_z \rangle$ contributes increasingly to the total spin $\langle I \rangle$ as compared to σ_{th}, resulting in the rapid rise of the alignment shown in fig. 12. However, in

the deep inelastic region where the total spin magnitude saturates, the increasing contribution of σ_{th} with the temperature causes $\langle I_z \rangle$ to slowly decrease. Correspondingly, the alignment, as measured by P_{zz}, decreases somewhat.

The values of $\langle I_z \rangle$ after neutron emission (curve 3) and of σ_n (curve 5) are also shown in fig. 13. The emission of a large number of neutrons removes substantial amounts of aligned spin, especially for large excitation energies. Since the alignment is a function of the ratio $\langle I_z \rangle/\sigma$, this result indicates that the contribution of neutron evaporation to the misalignment process is more a consequence of the reduction of $\langle I_z \rangle$ than of the increase of the variance caused by the introduction of σ_n^2. Finally, one should notice the different behaviors exhibited by the two components of the total variance σ^2. While the thermal component σ_{th}^2 is the dominant term over the whole Q-value range, its relative change with energy is much smaller than that of σ_n^2. The value of the ratio σ_{th}^2/σ_n^2 drops from approximately 46 to 3.6 in going from Q = -40 MeV to Q = -370 MeV.

In summary, the dependence of $\langle I \rangle$ and $\langle I_z \rangle$ on the reaction Q-value as well as the interplay between the primary and secondary misalignment mechanisms give rise to the following picture of the spin transfer process. At low Q-values, where σ_n is negligible, the rise of both the alignment and the γ-ray anisotropy is interpreted as due to the rapid buildup of aligned spin relative to the slow increase of σ_{th}. At large excitation energies, where the magnitude of the spin saturates, σ_n becomes comparable to σ_{th}. The increased total σ combined with the removal of aligned spin by neutron emission results in a substantial decrease of the alignment causing the anisotropy to plummet.

6. Conclusion

Continuum γ-ray multiplicity and anisotropy techniques have been used to study the magnitude and alignment of transferred angular momentum in the reaction $^{165}Ho + ^{165}Ho$ at 8.5 MeV/amu. A large anisotropy (~2) was observed at a Q-value of ~-150 MeV, whereas a low anisotropy was observed at much higher Q-values. This may be interpreted as being due to a change in nuclear spin alignment as a function of Q-value.

These data were compared to a statistical equilibrium model calculation which predicts the generation of random components of angular momentum introduced by the thermal excitation of angular-momentum-bearing collective modes. The fraction of statistical (E1) γ rays was extracted from the data and corrections for neutron emission were included in the calculations. These procedures significantly reduced two sources of uncertainty associated with previous works. Good agreement between experiment and theory was obtained only when the effects of thermally induced random-spin fluctuations were included in the calculations.

The following picture of the angular momentum transfer process emerges: At low Q-values, the transferred aligned angular momentum increases rapidly with increasing energy dissipation until it reaches a maximum at Q = ~-200 MeV. Within this region, the random spin components remain relatively small so the aligned spin component dominates and produces a large anisotropy for the observed γ rays. At larger Q-values, the increasing random-spin component limits the maximum nuclear alignment and thus the γ-ray anisotropy. The increasing numbers of emitted neutrons decrease the aligned spin and increase the random component. Thus, at the largest Q-values, the thermally induced random-spin component along with the effects of neutron emission combine to decrease the spin alignment substantially causing the observed γ-ray anisotropy to decrease to near unity.

The authors would like to acknowledge D.J. Morrissey, L.G. Sobotka, C.C. Hsu and H. Kluge for their help in the early stages of the experiment. We would also like to thank the staff of the SuperHILAC for delivering an excellent ^{165}Ho beam.

This work was supported by the Director, Office of Energy Research, Division of Nuclear Physics of the Office of High Energy and Nuclear Physics and Nuclear Sciences of the Basic Energy Sciences Program of the U.S. Department of Energy under Contract W-7405-ENG-48.

Table 1

Parameters of the Reaction
$^{165}Ho + ^{165}Ho$ at 8.5 MeV/amu

C.M. Energy	701 MeV
Coulomb Energy	419 MeV
Grazing Angle (Lab)	26°
ℓ_{max}	516 ħ
ℓ_{rms}	365 ħ

Table 2

Number of statistical transitions above 0.3 MeV, per fragment, extracted from the γ-ray spectra for different Q-value bins

Q (-MeV)	number of statistical transitions	fraction of the total number of transitions
20-59	1.4	0.29
60-103	1.5	0.16
104-147	2.2	0.16
148-191	2.5	0.16
192-232	2.7	0.17
233-276	2.7	0.18
277-325	2.7	0.19
326-425	2.7	0.20

Figure Captions

1. Top (a) and side (b) views of the experimental apparatus. Detectors labeled 1 and 3 are in the horizontal plane and detectors labeled 2 are in the vertical plane. An example of a deep-inelastic reaction producing projectile-like (P) and target-like (T) fragments in both a) the horizontal and b) vertical planes is shown.
2. TAC spectrum showing the separation of γ rays (γ) and neutrons (N) for the combination Si(1)-NaI(3) which exhibited the most neutron contamination. The vertical arrows on each side of the γ-ray peak show the gate used in sorting the data.
3. Schematic diagram of the modular electronics data acquisition system. The "ASC" in each linear channel is a combination of amplifier, SCA, and slow coincidence; G = linear gate, SD = scale-down logic signal, VT = valid-TAC logic, Tag (n) = Tagword logic, TS = TAC and SCA.
4. Laboratory energy spectra for Ho-like fragments detected at three angles.
5. Schematic diagram of the E^*-I plane showing the region populated by the ^{165}Ho + ^{165}Ho reaction at 8.5 MeV/amu. An example is shown for the decay of a QE event (a) and also for a DI event (b). The region populated by a representative compound-nucleus (CN) reaction is also shown. The projection on the ordinate represents the relative QE and DI cross sections observed at 27° in the lab. The lower detail stresses characteristics of the γ-ray decay process.
6. (a) Comparison of in-plane and out-of-plane γ-ray spectra in coincidence with fragments having a Q-value of $\sim$-125 MeV. Data points are shown only for the in-plane spectrum. (Note that the vertical scale of the corresponding figure which appears in ref. 26 is in error by a factor of 10.) (b) In-plane γ-ray spectra for various Q-value regions normalized to the average γ-ray multiplicity $\langle M_\gamma \rangle$.

7. Decomposition of the γ-ray spectrum to yield the number of statistical transitions (proportional to the area under the dashed line).

8. A comparison between the raw (squares) and "unfolded" (circles) γ-ray energy spectra.

9. Comparisons among the data at 23°, 27°, and 31° as a function of reaction Q-value. The top row represents $M_\gamma(90°)$ (filled circles), $M_\gamma(0°)$ (open circles), and the angle integrated γ-ray multiplicity $\langle M_\gamma \rangle$ for $E_\gamma > 0.3$ MeV (solid line). The center row shows the spin per fragment after neutron emission (solid line) derived from $\langle M_\gamma \rangle$ and the spin prior to neutron emission (dashed line). The bottom row shows the γ-ray anisotropy for the region $0.6 < E_\gamma < 1.2$ MeV.

10. A schematic diagram of the major time scales important to understanding the γ-ray anisotropy data and the reaction process.

11. Experimental and calculated values of the anisotropy vs Q-value for $E_\gamma > 0.6$ MeV. The solid line represents the complete calculation. The dotted line includes the secondary misalignment, and the dashed line represents full alignment. See text.

12. Extracted values of the alignment parameter P_{zz} plotted vs Q-value. The solid line represents a complete calculation, the dashed line does not include neutron effects, and the dotted line does not include the primary misalignment. See text.

13. The solid line (1) represents the spin transfer $\langle I \rangle$ before neutron emission at 27°. The dashed (2) and dotted (3) lines represent the extracted values of the aligned component $\langle I_z \rangle$ prior to neutron evaporation and of $\langle I_z \rangle$ after neutron emission, respectively. Line (4) represents the dispersion caused by the primary misalignment σ_{th}. Line (5) represents the dispersion due to neutron emission σ_n. See text.

References

1. M. Lefort and C. Ngô, Riv. Nuovo Cimento 2 (1979) 1 and references therein

2. M. Berlanger, M.A. Deleplanque, C. Gerschel, F. Hanappe, M. LeBlanc, J.F. Mayault, C. Ngô, D. Paya, N. Perrin, J. Péter, B. Tamain, and L. Valentin, Le Journal de Physique-Lettres 37 (1976) L323

3. R. Bock, B. Fischer, A. Gobbi, K. Hildenbrand, W. Kohl, U. Lynen, I. Rode, H. Stelzer, G. Auger, J. Galin, J.M. Lagrange, B.B. Back, and R. Albrecht, Nucleonika 22 (1977) 529

4. J.B. Natowitz, M.N. Namboodiri, P. Kasiraj, R. Eggers, L. Adler, P. Gonthier, C. Cerruti, and T. Alleman, Phys. Rev. Lett. 40 (1978) 751

5. C. Gerschel, M.A. Deleplanque, M. Ishihara, C. Ngô, N. Perrin, J. Péter, B. Tamain, L. Valentin, D. Paya, Y. Sugiyama, M. Berlanger, and F. Hanappe, Nucl. Phys. A317 (1979) 473

6. R.A. Dayras, R.G. Stokstad, C.B. Fulmer, D.C. Hensley, M.L. Halbert, R.L. Robinson, A.H. Snell, D.G. Sarantites, L. Westerberg, and J.H. Barker, Phys. Rev. Lett. 42 (1979) 697

7. P R Christensen, F. Folkmann, Ole Hansen, O. Nathan, N. Trautner, F. Videbaek, S.Y. van der Werf, H.C. Britt, R.P. Chestnut, H. Freiesleben, and F.Pühlhofer, Phys. Rev. Lett. 40 (1978) 1245

8. A. Olmi, H. Sann, D. Pelte, Y. Eyal, A. Gobbi, W. Kohl, U. Lynen, G. Rudolf, H. Stelzer, and R. Bock, Phys. Rev. Lett. 41 (1978) 688

9. R. Regimbart, A.N. Behkami, G.J. Wozniak, R.P. Schmitt, J.S. Sventek, and L.G. Moretto, Phys. Rev. Lett. 41 (1978) 1355

10. P. Dyer, R. J. Puigh, R. Vandenbosch, T.D. Thomas, M.S. Zisman, and L. Nunnelley, Nucl. Phys. A322 (1979) 205

11. D.v. Harrach, P. Glässel, Y. Civelekoglu, R. Männer, and H.J. Specht, Phys. Rev. Lett. 42 (1979) 1728

12. R.J. Puigh, P. Dyer, R. Vandenbosch, T.D. Thomas, L. Nunnelley and M.S. Zisman, Phys. Lett. 86B (1979) 24

13. Georg Wolschin, Nucl. Phys. A316 (1979) 146

14. S. Ayik, G. Wolschin, and W. Nörenberg, Z. Physik A286 (1978) 271

15. L.G. Moretto and R.P Schmitt, Phys. Rev. C21 (1980) 204

16. R.A. Dayras, R.G. Stokstad, D.C. Hensley, M.L. Halbert, D.G. Sarantites, L. Westerberg, and J.H. Barker, Phys. Rev. C22 (1980) 1485

17. K. Van Bibber, R. Ledoux, S.G. Steadman, F. Videbaek, G. Young and C. Flaum, Phys. Rev. Lett. 38 (1977) 334

18. C. Lauterbach, W. Dünnweber, G. Graw, W. Hering, H. Puchta, and W. Trautmann, Phys. Rev. Lett. 41 (1978) 1774

19. H. Puchta, W. Dünnweber, W. Hering, C. Lauterbach, and W. Trautmann, Phys. Rev. Lett. 43 (1979) 623

20. P. Aguer, R.P. Schmitt, G.J. Wozniak, D. Habs, R.M. Diamond, C. Ellegaard, D.L. Hillis, C.C. Hsu, G.J. Mathews, L.G. Moretto, G.U. Rattazzi, C.P. Roulet, and F.S. Stephens, Phys. Rev. Lett. 43 (1979) 1778

21. R.J Puigh, H. Doubre, A. Lazzarini, A. Seamster, R. Vandenbosch, M. Zisman, and T.D. Thomas, Nucl. Phys. A336 (1980) 279

22. H. Esbensen, A. Winther, R.A. Broglia and C.H. Dasso, Phys. Rev. Lett. 41 (1978) 296

23. R. Vandenbosch, Phys. Rev. C20 (1979) 171

24. F.S. Stephens, Lawrence Berkeley Laboratory report LBL-10356, published in the proceedings of the Varenna Conf., Varenna, Italy, July 1979

25. R.M. Diamond and F.S. Stephens, Annual Review of Nuclear and Particle Science 30 (1980) 85, Annual Review, Inc., Palo Alto, CA.

26. G.J. Wozniak, R.J. McDonald, A.J. Pacheco, C.C. Hsu, D.J. Morrissey, L.G. Sobotka, L.G. Moretto, S. Shih, C. Schück, R.M. Diamond, H. Kluge, and F.S. Stephens, Phys. Rev. Lett. 45 (1980) 1081

27. J. B. Moulton, J.E. Stephenson, R.P. Schmitt, and G.J. Wozniak, Nucl. Inst. Meth. 157 (1978) 325

28. L.C. Northcliffe and R.F. Schilling, Nucl. Data Tables A7 (1970) 233

29. T.K. Alexander and J.S. Forster, Advances in Nucl. Phys. V10 (1978) Ch. 3, Plenum Press, New York

30. C. Maples and J. Sivak, Computerized Data-Acquisition Systems in Particle and Nuclear Physics, LBL-9182 unpublished, Conf. Santa Fe, NM, May 14-17, 1979

31. A. Holm, IEEE Transactions on Nuclear Science, NS26 (1979) 4569

32. M. Neiman, Lawrence Berkeley Laboratory, PUB 3014 (1981)

33. P. Russo, R.P. Schmitt, G.J. Wozniak, R.C. Jared, P. Glässel, B. Cauvin, J.S. Sventek and L.G. Moretto, Nucl. Phys. A281 (1977) 509

34. M.A. Deleplanque, Th. Byrski, R.M. Diamond, H. Hübel, F.S. Stephens, B. Herskind, and R. Bauer, Phys. Rev. Lett. 41 (1978) 1105

35. R.S. Simon, M.V. Banaschik, R.M. Diamond, J.O. Newton, and F.S. Stephens, Nuclear Physics A290 (1977) 253

36. H.J. Körner, D.L. Hillis, C.P. Roulet, P. Aguer, C. Ellegaard, D.B. Fossan, D. Habs, M. Neiman, F.S. Stephens and R.M. Diamond, Phys. Rev. Lett. 43 (1979) 490

37. S.J. Feenstra, J. van Klinken, J.P. Pijn, R. Janssens, C. Michel, J. Steyaert, J. Vervier, K. Cornelis, M. Huyse, and G. Lhersonneau, Phys. Lett. 80B (1979) 183

38. S.H. Sie, J.O. Newton, J.R. Leigh and R.M. Diamond, Phys. Rev. Lett. 46 (1981) 405

39. J.F. Mollenauer, Phys. Rev. 127 (1962) 867

40. M.N. Namboodiri, J.B. Natowitz, P. Kasiraj, R. Eggers, L. Adler, P. Gonthier, C. Cerruti, and S. Simon, Phys. Rev. C 20 (1979) 982

41. C.M. Lederer and V.S. Shirley, eds., Table of Isotopes, seventh edition, John Wiley & Sons, Inc., New York (1978) ISBN #0-471-04180-7

42. S.K. Blau and L.G. Moretto, Nucl. Phys. A359 (1981) 477

43. S.R. de Groot, H.A. Tolhoek, W.J. Huiskamp, in Alpha-, Beta- and Gamma-ray Spectroscopy, ed. K. Siegbahn, Vol. 2 (North-Holland, Amsterdam (1966) p. 1199

44. J.R. Huizenga and R. Vandenbosch, Nuclear Fission, Academic Press, New York, 1973, ISBN #0-12-710850-5

45. L.G. Moretto, S.K. Blau, and A.J. Pacheco, Lawrence Berkeley Laboratory report LBL-10805, Nucl. Phys. (in press)

46. R. Nordhagen, G. Goldring, R.M. Diamond, K. Nakai, and F.S. Stephens, Nucl. Phys. A142 (1970) 577

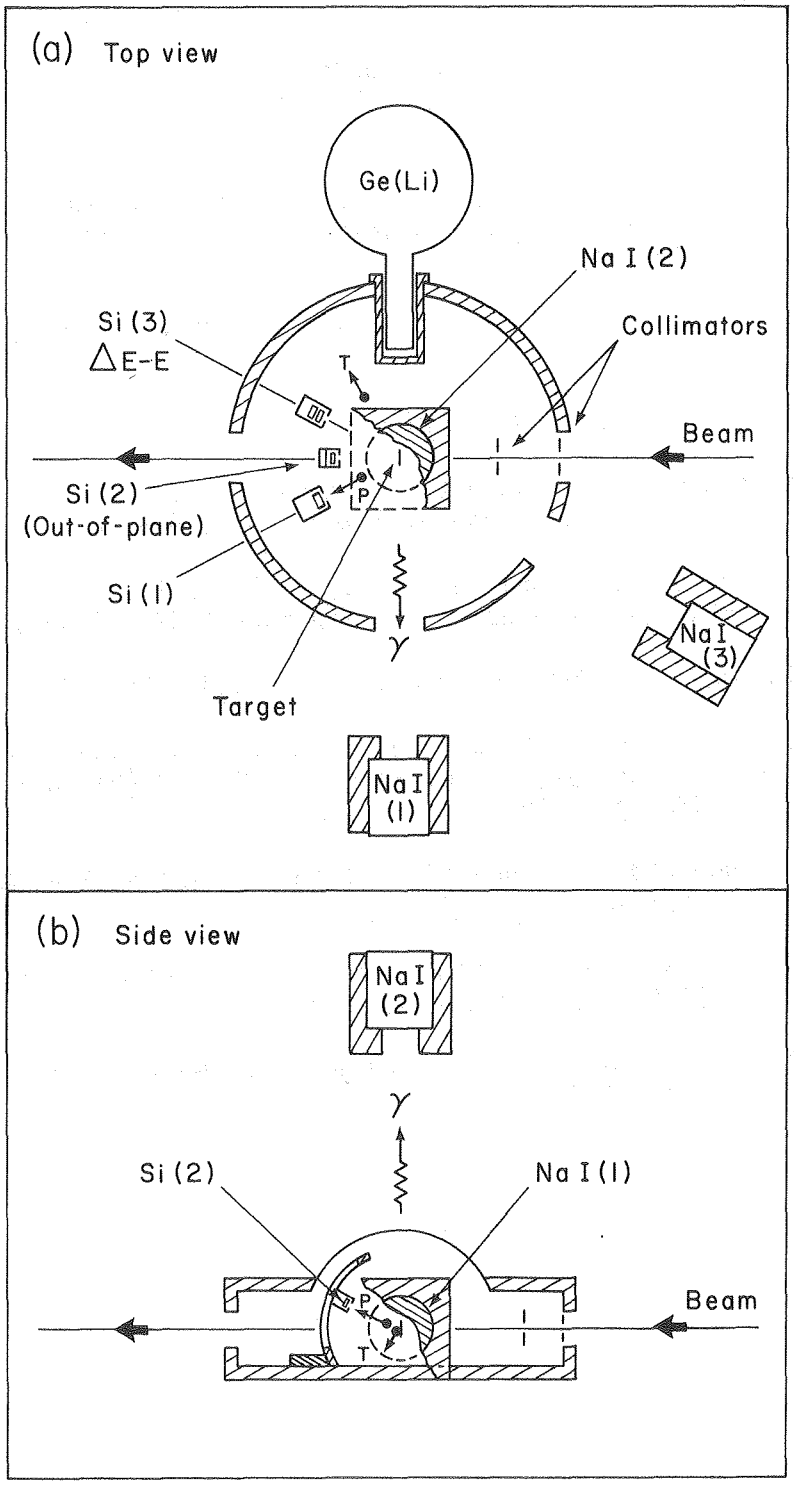

XBL 8010-2160

Fig. 1

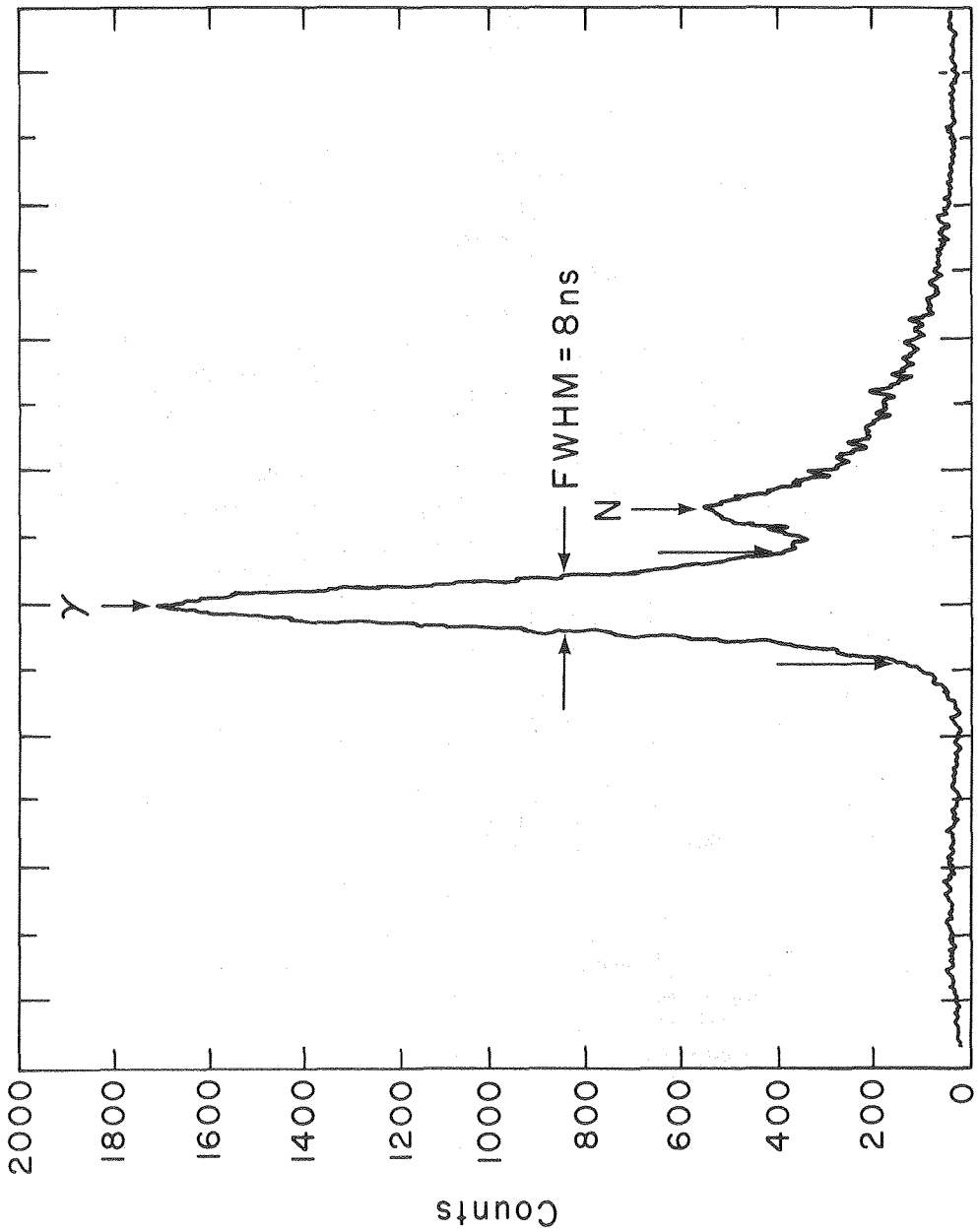

XBL 8010-2178

Fig. 2

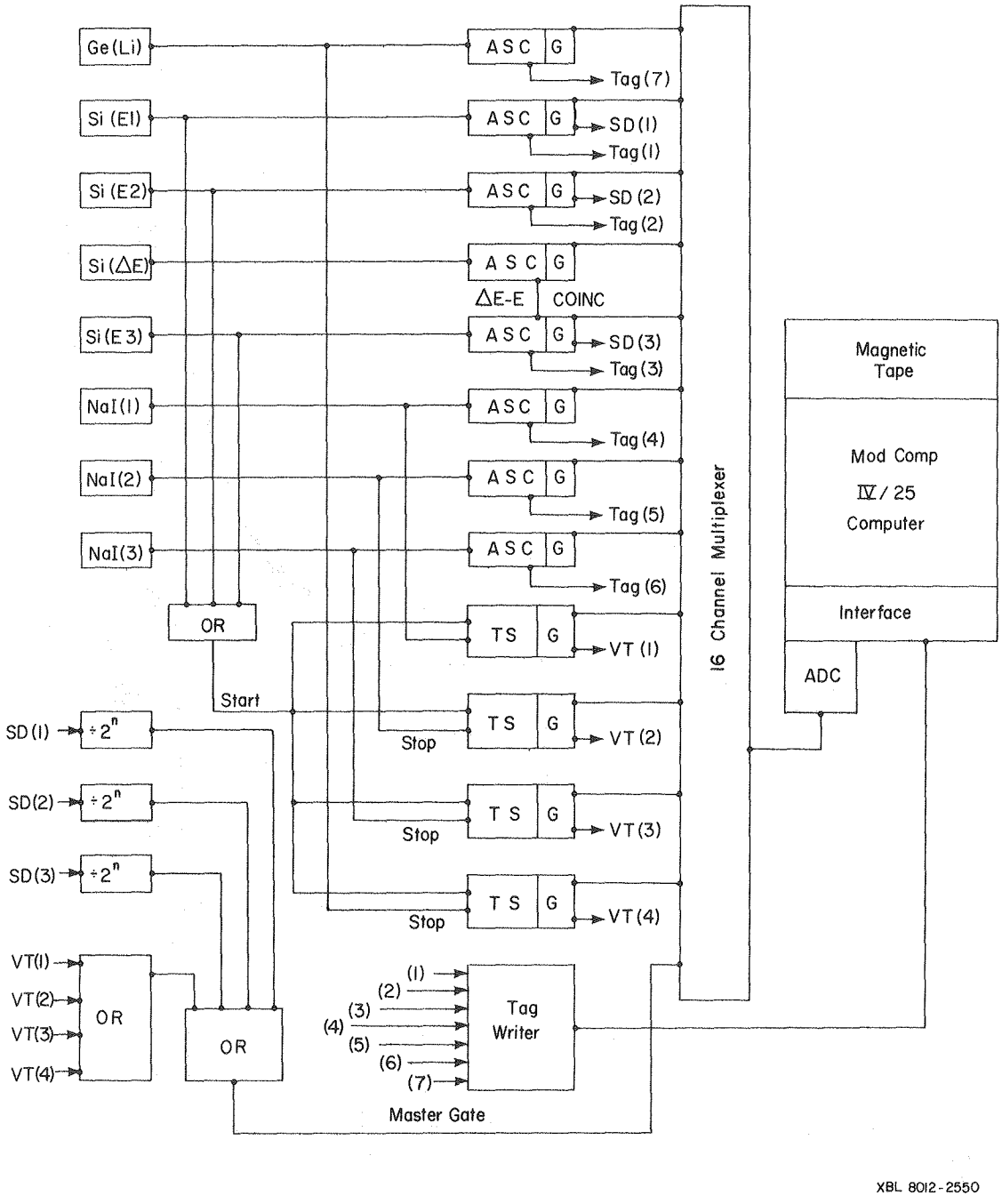
Ge(Li)
Si (E1)
Si (E2)
Si (ΔE)
Si (E 3)
NaI(1)
NaI(2)
NaI(3)
A S C
G
Tag(7)
SD(1)
Tag(1)
SD (2)
Tag(2)
ΔE-E
COINC
SD(3)
Tag(3)
Tag(4)
Tag(5)
Tag(6)
OR
TS
VT (1)
Start
Stop
VT (2)
T S
VT(3)
VT (4)
SD(1)
SD(2)
SD(3)
÷2ⁿ
VT(1)
VT(2)
VT(3)
VT(4)
(1)
(2)
(3)
(4)
(5)
(6)
(7)
Tag
Writer
Master Gate
16 Channel Multiplexer
Magnetic
Tape
Mod Comp
IV / 25
Computer
Interface
ADC
XBL 8012-2550

Fig. 3

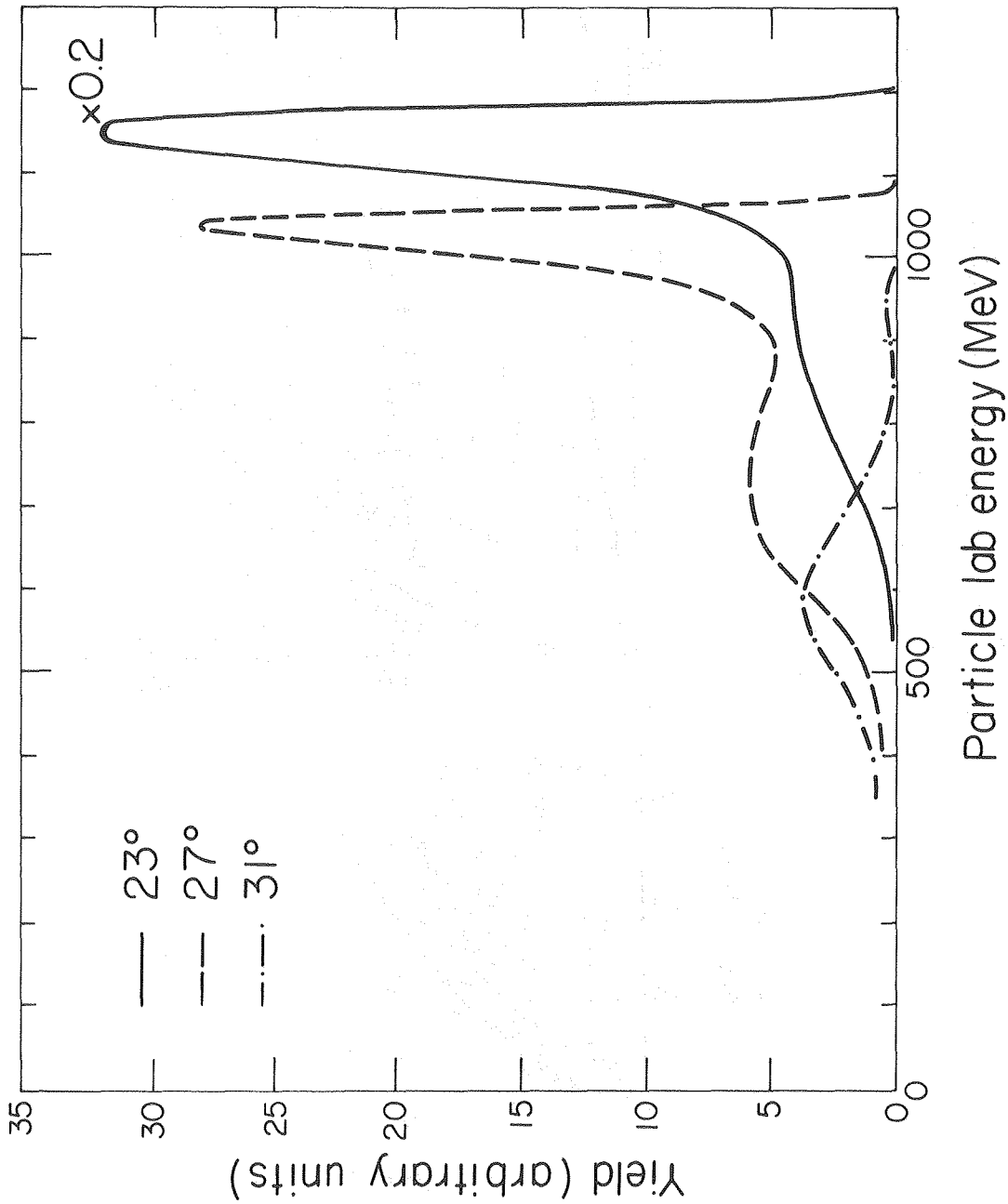

XBL 814-2261

Fig. 4

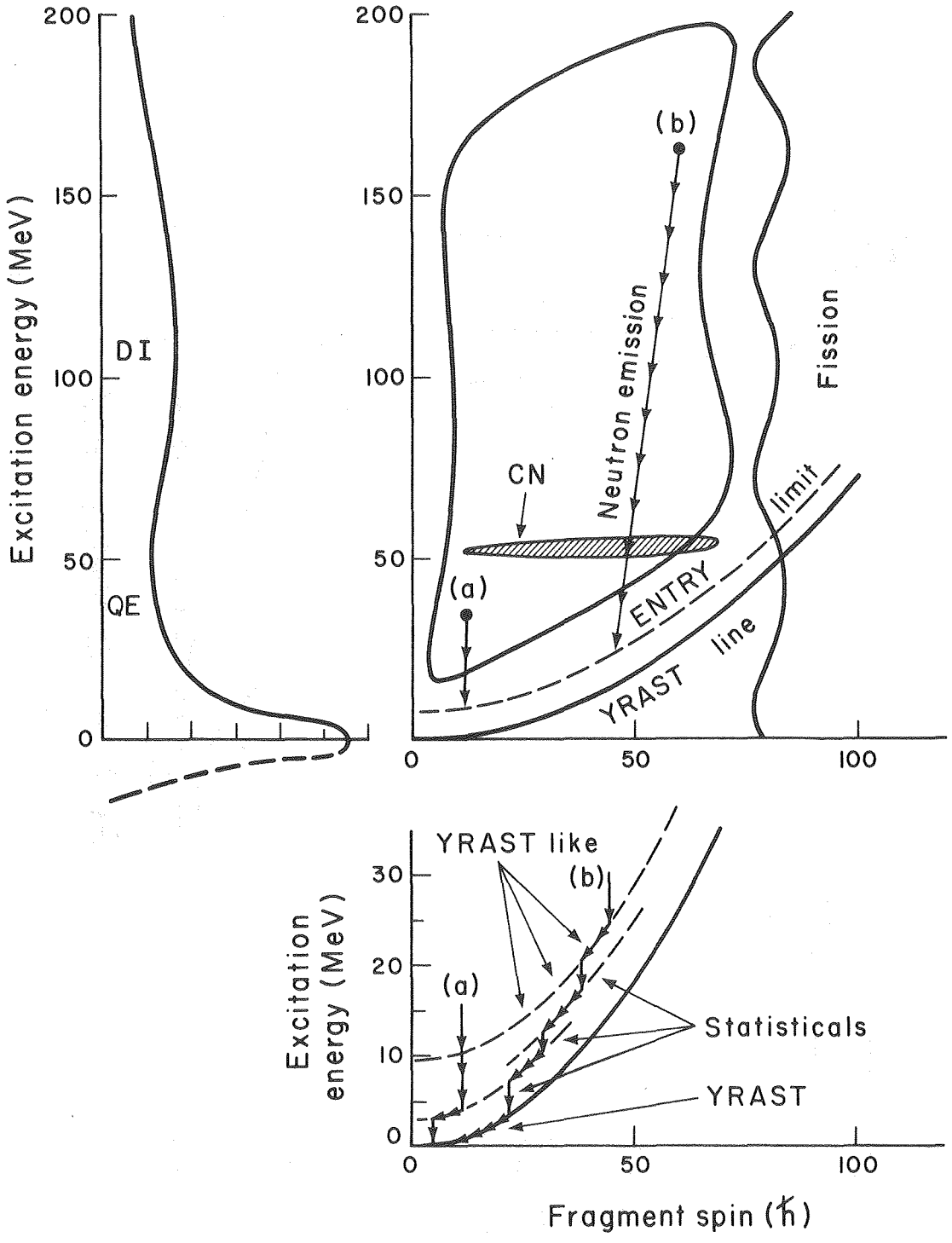
200
150
100
50
0
Excitation energy (MeV)
DI
QE
200
150
100
50
0
50
100
(b)
Neutron emission
Fission
CN
limit
(a)
ENTRY
YRAST line
YRAST like
(b)
30
20
10
0
Excitation energy (MeV)
(a)
Statisticals
YRAST
0
50
100
Fragment spin (ħ)
XBL 8010-2179

Fig. 5

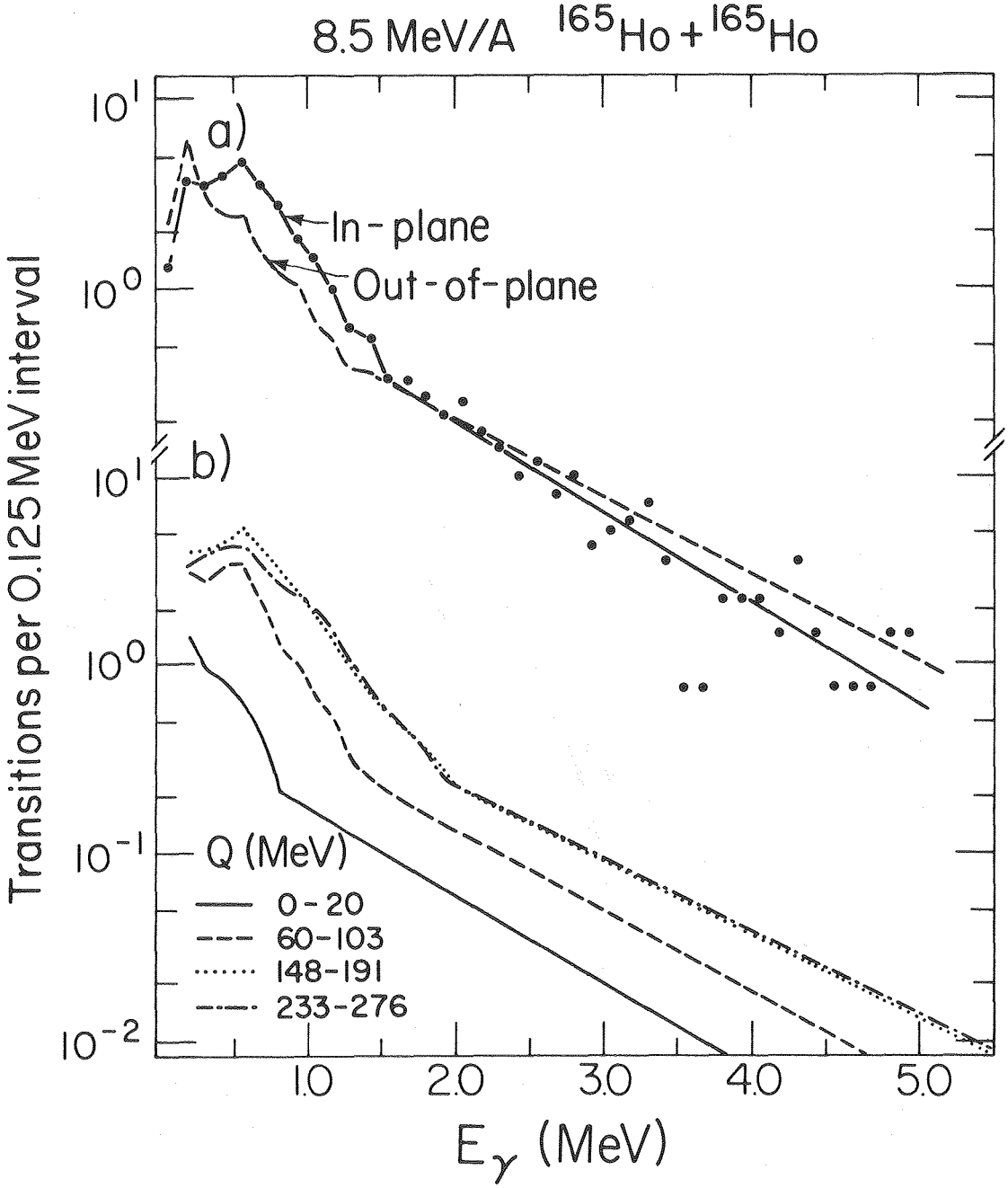

XBL 806-1194B

Fig. 6

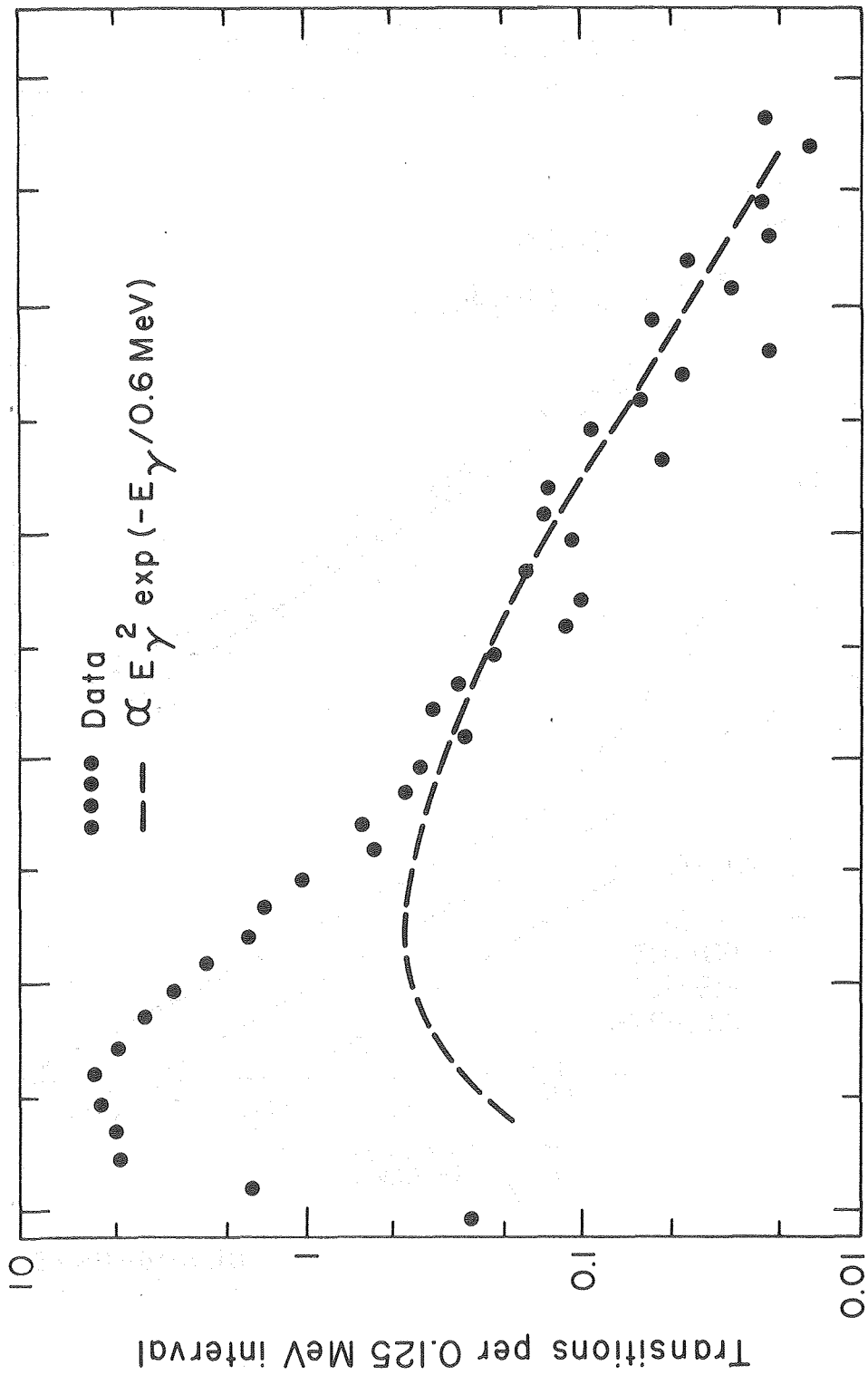

XBL 8010-2159

Fig. 7

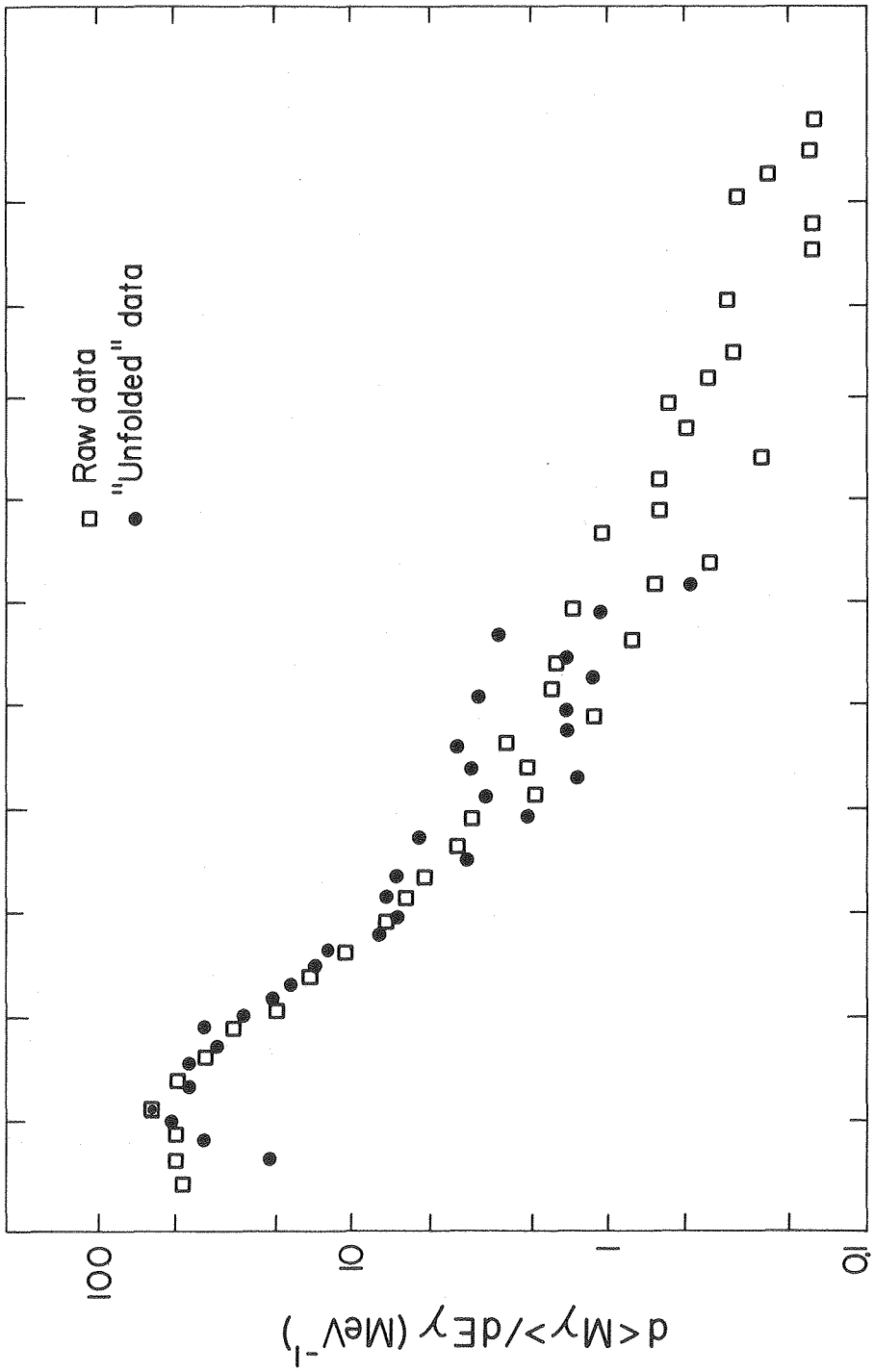

XBL 8012-2549

Fig. 8

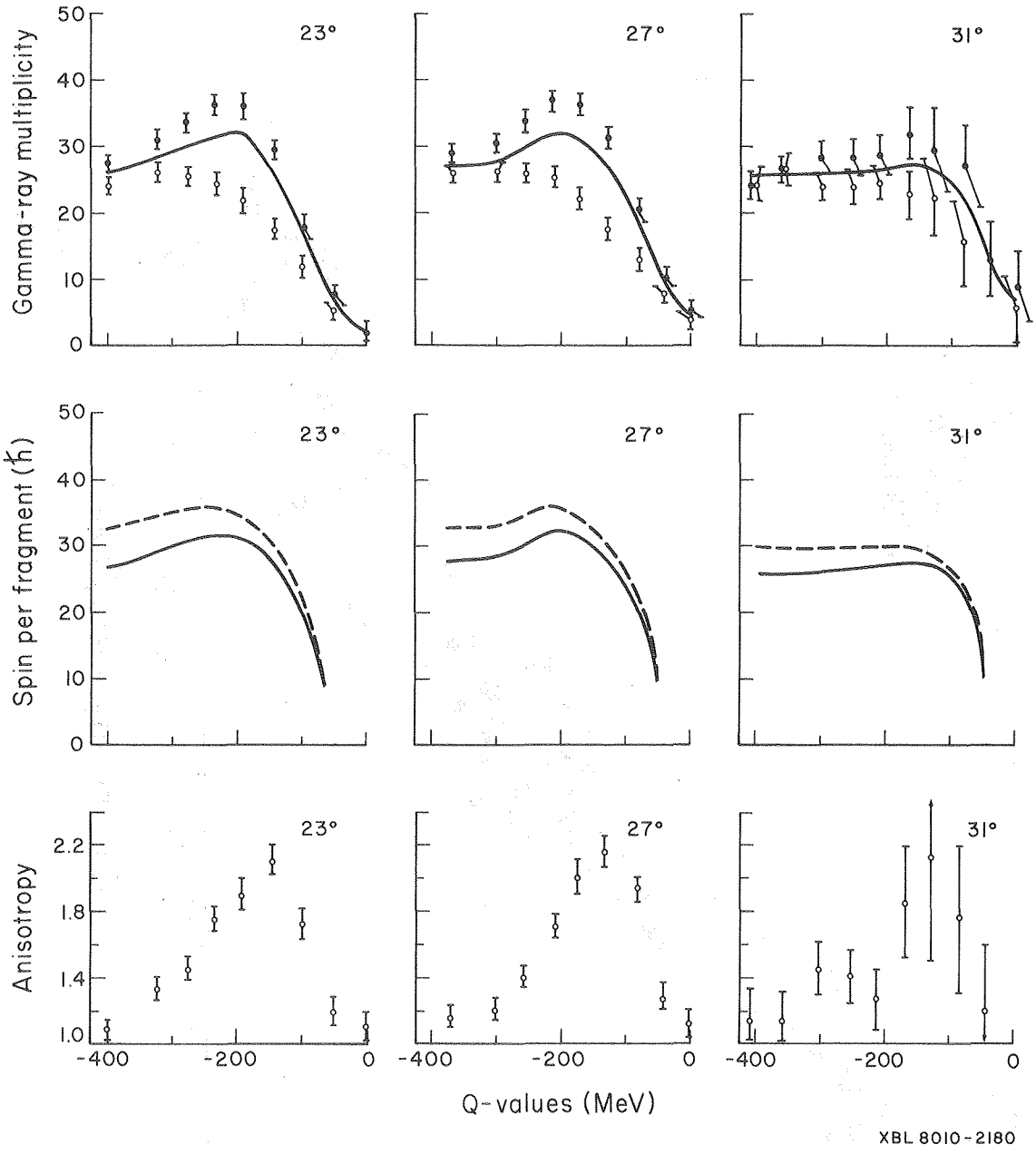
Gamma-ray multiplicity
Spin per fragment (ħ)
Anisotropy
23°
27°
31°
Q-values (MeV)
XBL 8010-2180

Fig. 9

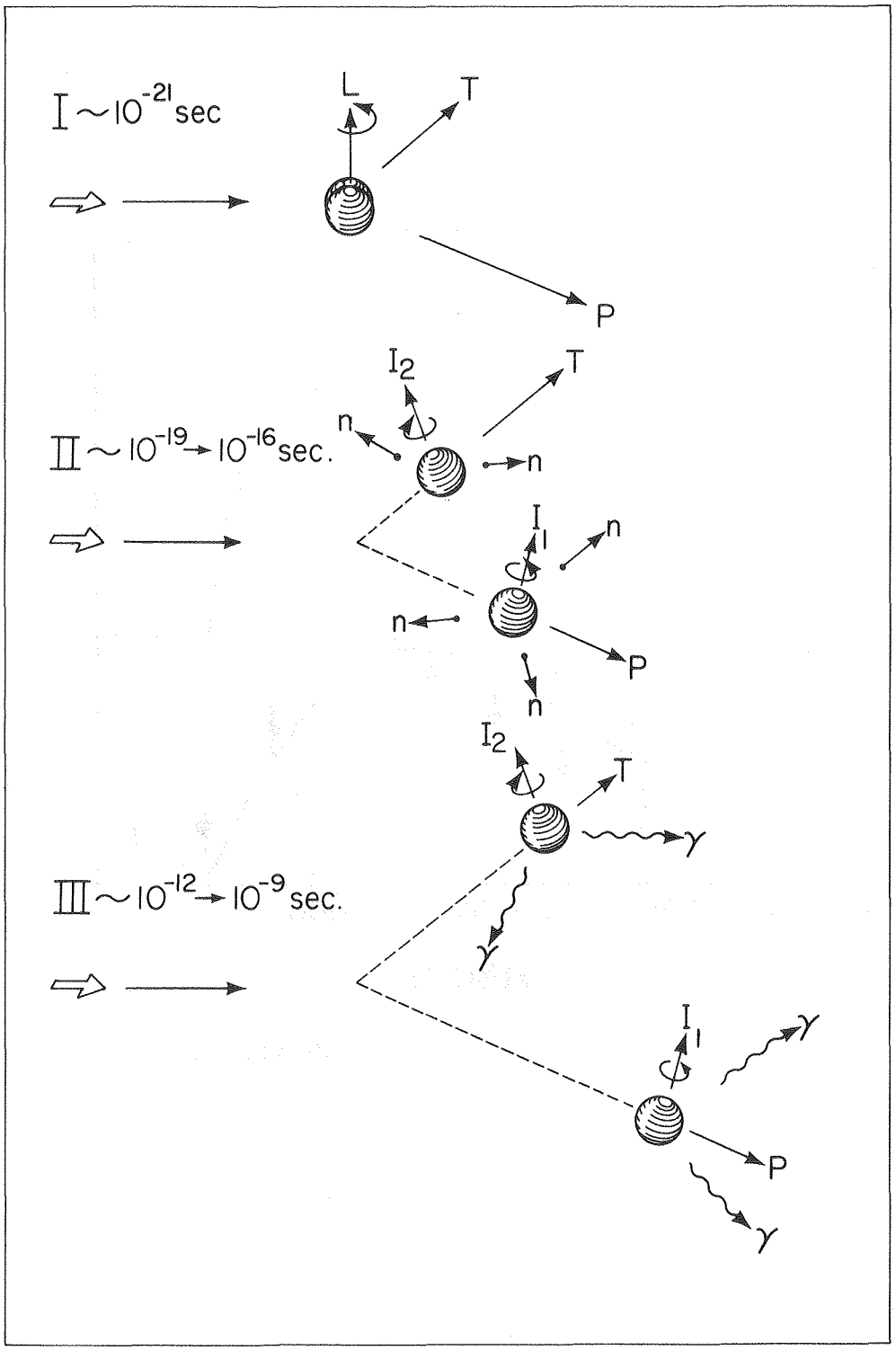

XBL 8012-2547

Fig. 10

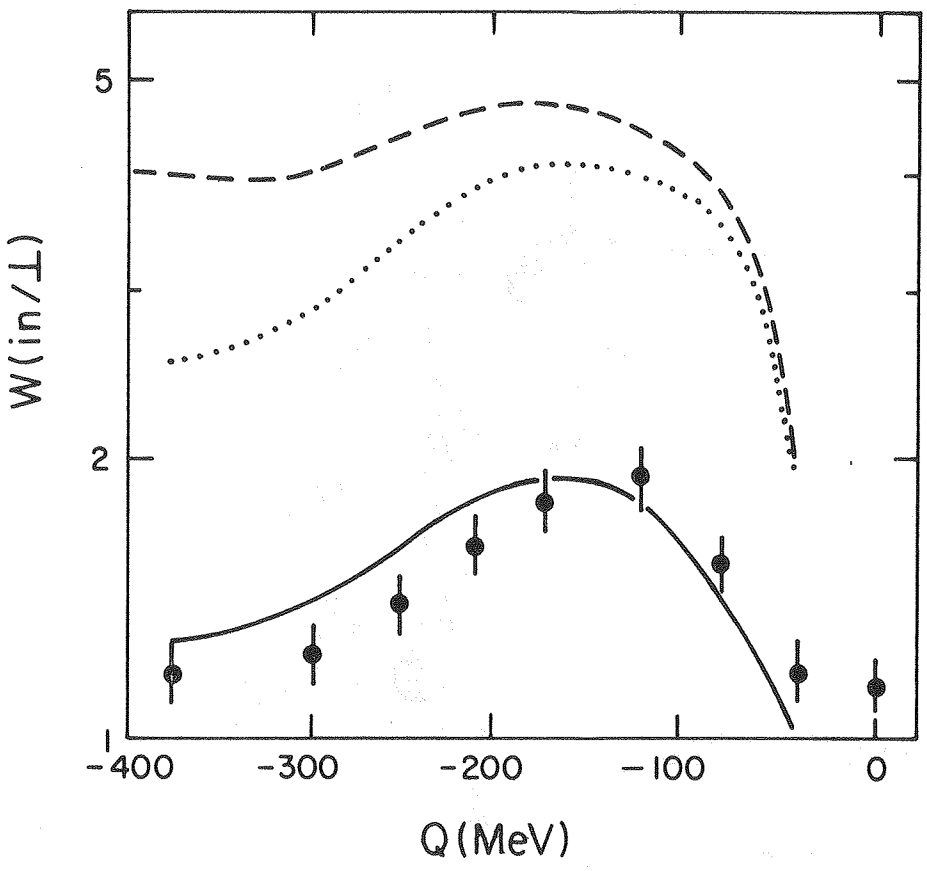

XBL814-2229

Fig. 11

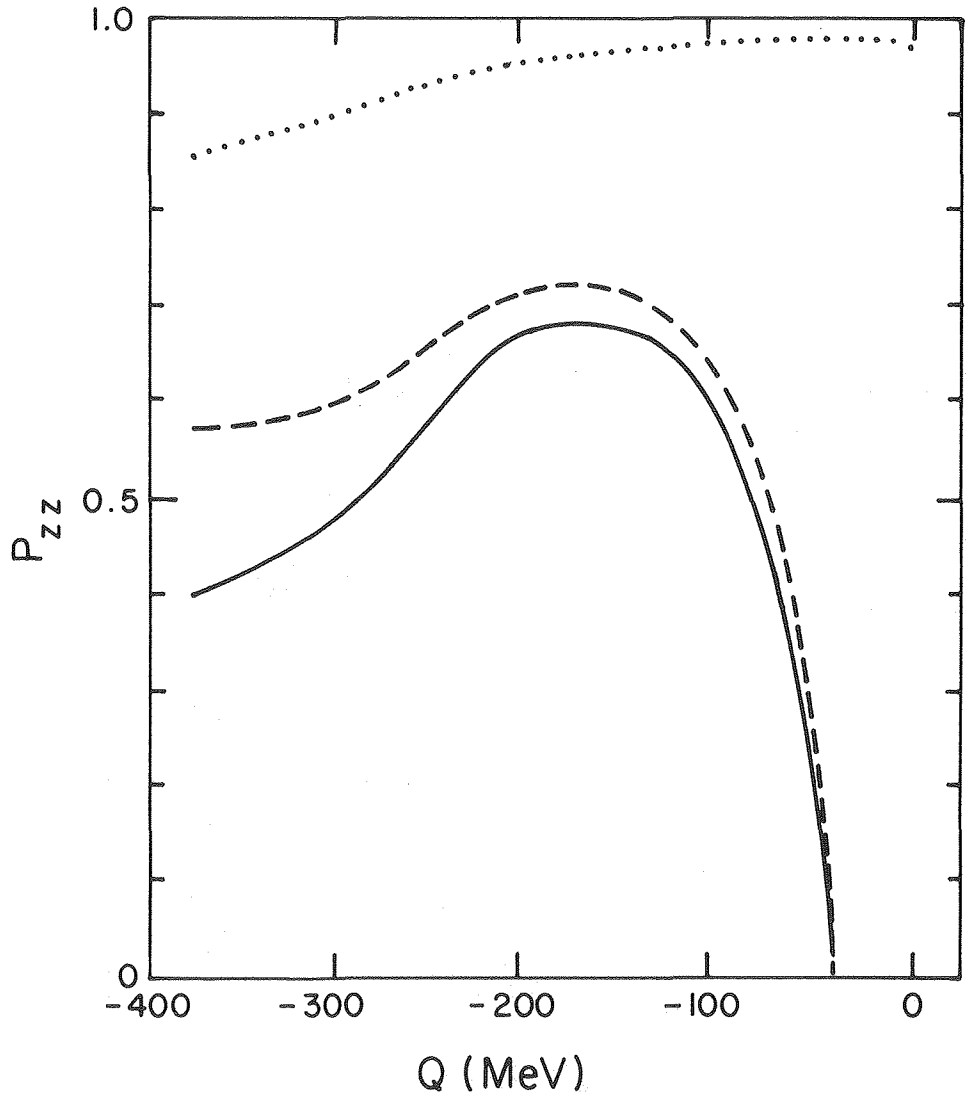

XBL814-2230

Fig. 12

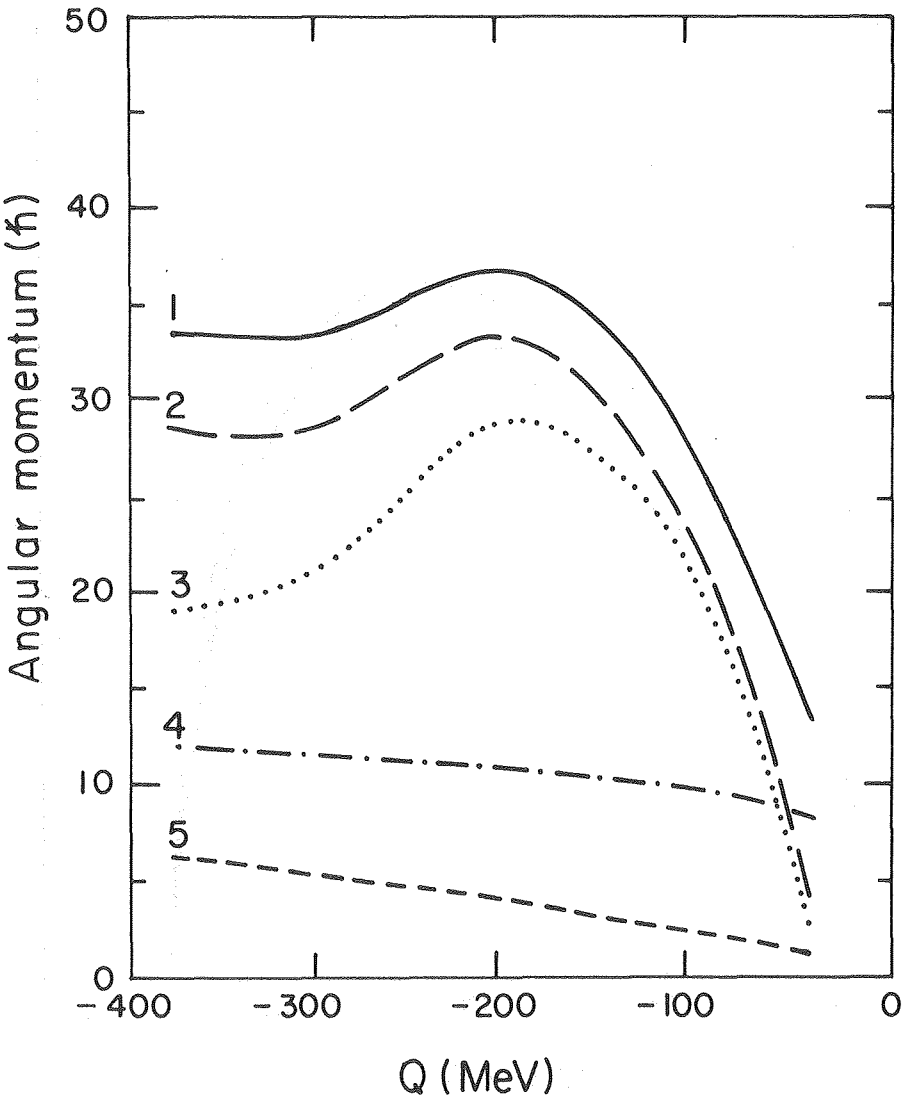
50
40
30
20
10
0
Angular momentum (ħ)
1
2
3
4
5
-400
-300
-200
-100
0
Q (MeV)
XBL 814-2231

Fig. 13